



A combined digital image correlation/particle image velocimetry study of water-backed impact

Peng Zhang^a, Maurizio Porfiri^{a,b,*}

^a Department of Mechanical and Aerospace Engineering, New York University Tandon School of Engineering, Six MetroTech Center, Brooklyn, NY 11201, USA

^b Department of Biomedical Engineering, New York University Tandon School of Engineering, Six MetroTech Center, Brooklyn, NY 11201, USA



ARTICLE INFO

Keywords:

Fluid-structure interaction
Hydrodynamic loading
Impulsive loading
Simultaneous measurement
Structural dynamics

ABSTRACT

Several aeronautical and naval structures are routinely exposed to impulsive loading conditions that elicit complex fluid-structure interactions. An archetypal problem that has attracted considerable attention is the impact on a compliant plate, fixed on a water surface. Despite significant progress in mathematical modeling of the impact, several technical questions remain open due to the lack of a simultaneous experimental characterization of the structural response and fluid flow. Here, we seek to fill this gap of knowledge through the integration of digital image correlation (DIC) and particle image velocimetry (PIV). We employ DIC to measure the apparent in-plane displacement of the plate, from which we reconstruct its out-of-plane deflection. On the other hand, PIV is utilized to measure the velocity field of the water, from which we infer the pressure field in the fluid and the hydrodynamic loading on the plate. We examine a number of aggregated measures, including the mid-span deflection, strain energy stored in bending and stretching of the plate, modal contribution factors, hydrodynamic loading, and added mass coefficient. Just as our approach constitutes a significant methodological step forward in the study of unsteady fluid-structure interactions, our experimental results contribute new evidence for an improved understanding of water-backed impact.

1. Introduction

Understanding fluid-structure interaction associated with water-backed impact is critical to the design of naval and aerospace structures. A tool falling on a panel of a boat hull [1,2] and an aircraft landing on aircraft carriers or floating airports [3–5], are classical examples of water-backed impact. To elucidate the physical mechanisms underlying water-backed impact, several authors have examined the archetypal problem of the impact on a compliant plate fixed on the surface of water [2,6–10]. As detailed in [6], highly-controllable experimental conditions could be attained by modifying traditional drop-weight impact setups to include a water chamber for the specimen to be fixed upon. By measuring the contact force and the specimen deformation through the instrumented impactor, it is possible to examine the dynamic response of water-backed specimens of different geometry and composition [2,7–10].

Contrasting results have been reported on the role of the fluid-structure interaction in water-backed impact. Water-backed metal beams have been found to exhibit less severe deformation than air-backed beams, due to added mass effect [11]. Further evidence in favor

of the added mass effect can be found in [12], where water-backed composite plates have been shown to experience larger impact forces than air-backed plates. Conflicting findings have been recently reported on the dynamic response of composite plates, where water-backing was found to increase deformation [2]. The surprising findings have been associated with the occurrence of material damages in the composites during impact, which could reduce the sample stiffness [8] and, consequently, increase the deformation.

Supported by these experimental efforts, several modeling frameworks have been proposed to explain the fluid-structure interaction during impact. Focusing on two-dimensional deformations, various authors have proposed simplified structural models based on Euler-Bernoulli beam undergoing pure bending [13,14] and, potentially, membrane-stiffening for large deformations [15]. By projecting the deflection of the plate on its fundamental in-vacuum mode shape, a simplified one-degree-of-freedom system has been developed to describe the dynamic response of the plate [15–17]. The flow field below the plate has been modeled through potential flow theory [13–15], to quantify the distributed hydrodynamic loading acting on the structure. Due to their mathematical tractability, these modeling efforts offer a

* Corresponding author at: Department of Mechanical and Aerospace Engineering and Department of Biomedical Engineering, New York University Tandon School of Engineering, Six MetroTech Center, Brooklyn, NY 11201, USA.

E-mail address: mporfiri@nyu.edu (M. Porfiri).

promising lens through which one can examine water-backed impact and systematically explore the role of physical and geometric properties.

However, two key experimental limitations are presently challenging the validation of these modeling schemes. First, experimental measurements of water-backed impact have been largely limited to point-wise recordings of the contact force, plate deflection, and hydrodynamic pressure [2,8,11,18,19]. Although such measurements are of critical value, the lack of distributed structural data hinders the validation of structural models. Second, the lack of data on the flow physics associated with the impact challenges the verification of predictions on the hydrodynamic loading experienced during impact. These limitations could be mitigated by attempting at the simultaneous, full-field measurements of both the plate deformation and the fluid flow. Such an experimental backdrop could assist in the validation of theoretical models and improve our understanding of the fluid-structure interaction. The objective of this work is to develop a combined experimental framework, based on the integration of digital image correlation (DIC) and particle image velocimetry (PIV), for the study of water-backed impact.

The structural response of the plate was measured by two-dimensional DIC using a single high-speed camera. DIC is a non-invasive experimental technique for the quantification of the displacement and strain field on the surface of solids [20,21]. In a DIC experiment, a camera is employed to record images of random speckle patterns applied on the surface of the structure. The displacement and the strain field of the structure are obtained through cross-correlation of the speckle patterns before and after deformation [21]. In the past, DIC has facilitated the study of several impact problems, by affording the precise quantification of the mechanical deformation of structures at a fast time scale and fine spatial resolution [22–26]. Here, DIC was employed to pinpoint the key differences between the deformations elicited by water- and air-backed impact, thereby elucidating the role of water-backing. From DIC-based measurements, we analyzed the extent of membrane-stiffening through the computation of the elastic energy associated with bending and membrane-stretching. We also leveraged DIC-based data to conduct a modal analysis of the structural dynamics, toward an assessment of the validity of single-mode shape approximation, as commonly proposed in the literature [15–17].

The flow physics associated with the impact was quantified through planar two-dimensional PIV [27,28]. Briefly, in a PIV experiment, the fluid is seeded with micro-particles, and is illuminated on a two-dimensional plane by a laser sheet. A high-speed camera is used to record consecutive images of the particles, which are subsequently processed by cross-correlation within interrogation windows on each image [28]. In the literature, PIV has been employed in several studies on the impact of structures [29]. In this work, PIV was utilized to measure the fluid velocity below the plate, from which we reconstructed the pressure field, by solving the Poisson equation [30,31]. The hydrodynamic loading on the plate was then extracted from the pressure to clarify the fluid-structure interaction and help quantify the added mass phenomenon.

To the best of our knowledge, a combined DIC/PIV approach has never been attempted for the study of unsteady fluid-structure interaction associated with water-backed impact. The premise of a combined DIC/PIV for the study of fluid-structure interactions has been demonstrated in our recent work [32], in which the static deformation and hydrodynamic loading on a plate placed in a steady cross-flow were analyzed. With respect to [32], several technical improvements and modifications were needed to tackle water-backed impact. First, we pursued an indirect approach for DIC, where the camera recorded the apparent in-plane movement of the top surface of the plate [33,34] rather than the out-of-plane deflection as in [32]. In this way, we were able to mitigate the effect of water splash, surface waves, air ventilation, and image blurring due to limited camera depth-of-field, which would have emerged by recording from the side-view. Second,

interference between the acquisition of DIC and PIV was resolved by installing light filters on cameras, which selectively recorded light at different emission wavelengths. Finally, DIC and PIV cameras were controlled to acquire images simultaneously with a high temporal resolution to address the highly unsteady nature of the impact.

The main contributions of this work include: (i) the development of a novel experimental framework for the simultaneous quantification of the structural dynamics and the flow physics in unsteady fluid-structure interaction problems; (ii) the first quantification of the flow field, in terms of both velocity and pressure, caused by water-backed impact; (iii) the first set of distributed measurements of the deflection field of a water-backed plate; and (iv) the detailed analysis of a wide range of aggregate experimental variables that should help in the validation of mathematical models of water-backed impact. The rest of the paper is organized as follows: the experimental design of the combined DIC/PIV is detailed in Section 2; the analysis method is presented in Section 3; the main results of our experiments are presented and discussed in Section 4; and conclusions from our main findings are drawn in Section 5.

2. Experimental design

We investigated the fluid-structure interaction associated with the impact on a flexible plate resting on a water surface, as sketched in Fig. 1(a). Specifically, a plate with half-length $L = 9.5$ cm, thickness $h = 1.0$ cm, and width $b = 6.0$ cm was clamped at both ends to rest on the water surface of a transparent tank. The tank, measuring $80 \times 32 \times 35$ cm (length×width×depth), was filled with water at a depth of 20 cm, so that the bottom surface of the plate was leveled with the water surface. All the experiments were conducted at room temperature, such that the density and dynamic viscosity of water were $\rho = 1.0 \times 10^3$ kg/m³ and $\mu = 1$ mPa s, respectively.

The plate was fabricated with a highly flexible material, Polydimethylsiloxane (PDMS). First, a SYLGARD 184 Silicone base and curing agent (The Dow Chemical Company, material number 1673921) in their liquid state were mixed with a 10:1 ratio. The mixture was then cast into a 3D-printed mold, and then left to polymerize at 60 °C for 12 h. The polymerized PDMS had an effective Young's modulus of $E = 1.58$ MPa¹ and mass density of $\rho_b = 1.02 \times 10^3$ kg/m³[36–38].

A drop tower of 1 m in height was assembled beside the water tank using aluminum frames. The same drop tower has been used in our previous studies on water entry problems [39]. A cylindrical-shaped impactor was 3D-printed with Polylactic Acid. The shape of the impactor was selected to elicit a uniform load along the width of the plate, thereby reducing the extent of three-dimensional phenomena in the fluid-structure interaction. The impactor was attached to a vertical rail through an L-shaped connector, which guided the free fall of the impactor and ensured that the impact would take place at the mid-span of the plate. The total mass of the impactor and the connector was $M = 231.7$ g. The impactor was held in place at a given distance from the plate by an electromagnet (SECO-LARM, model E-941SA-80Q), prior to each experimental trial. The drop height of the impactor was varied from 1 cm to 10 cm to obtain a nominal impact velocity between 0.44 m/s and 1.41 m/s.

A major contribution of the current work is the implementation of

¹ The effective Young's modulus of the plate was determined through a static calibration test, where a series of weights of mass, m , ranging from 8.6 to 34.9 g, were applied at the mid-span of the plate. The weights caused a mid-span deflection, δ , between 0.39 mm and 1.55 mm, measured from a side-view camera. The value of E was then determined using a linear regression on the analytical relation between the mid-span deflection and the applied load based on Euler-Bernoulli beam theory, $\delta = \frac{mgL^3}{2Ebh^3}$, where g is gravitational acceleration. While a nonlinear constitutive law should be generally preferred for PDMS, the moderate strain levels experienced in our experiments justify the use of a simpler linear model [35].

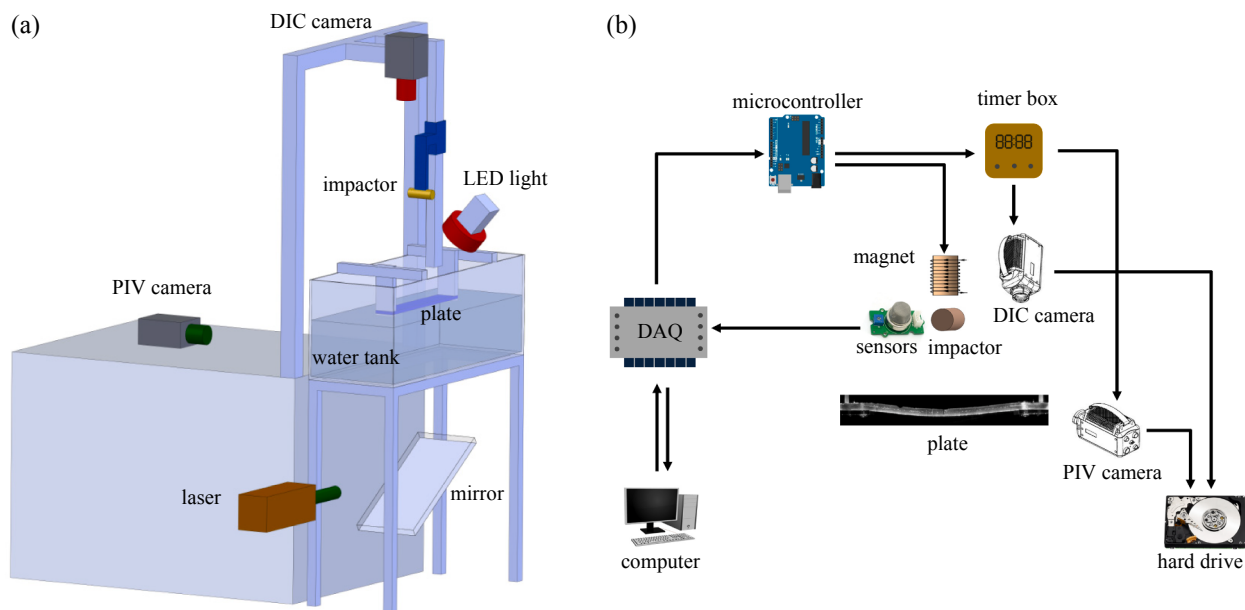


Fig. 1. (a) Schematic of the experimental setup. (b) Diagram of the hardware control and data acquisition scheme.

PIV and DIC for the simultaneous quantification of the flow physics and structural response of the unsteady fluid–structure interaction problem. PIV was employed to study the flow physics during impact. Polyamide particles (PSP-50, Dantec Dynamics) with a mean diameter of 50 μm and density of $1.0 \times 10^3 \text{ kg/m}^3$ were used as seeding particles. A Dantec PIV system (Dantec Dynamics) was utilized to acquire time-resolved particle images during impact. The PIV system consisted of a 532 nm wavelength, 5 W maximum power continuous wave Nd:YAG laser (RayPower 5000, Dantec Dynamics), a high speed camera (Phantom SpeedSense, Vision Research), and a timer box (80N77, Dantec Dynamics). A laser sheet was generated below the water tank, which was then reflected upwards by a mirror placed at a 45° angle beneath the water tank to create a two-dimensional laser plane perpendicular to the plate, at the middle of its width. The PIV camera had a resolution of 1632 \times 1200 pixels and a field of view of around 30.3 \times 22.3 cm. Due to the symmetry of the problem, we acquired data for only half of the plate and the water below it. The PIV camera was set to acquire images at a rate of 1000 Hz with exposure time of 1000 μs . The camera was fitted with a band-pass filter with a center wavelength of 532 nm and a bandwidth of 10 nm, to selectively record light only at the laser emission wavelength.

DIC was employed to study the structural response of the plate during impact. The deflection of the plate was indirectly reconstructed from the apparent in-plane displacement of the plate top surface. Prior to experimental trials, a uniform layer of red silicone paint (Smooth-On, Inc., platinum silicone base paint mixed with red pigment) was applied on the top surface of the plate. Upon drying of the red silicone paint, a blue acrylic paint was sprayed uniformly on top and was left to dry for 24 h. The color of the paints was selected to produce a high contrast speckle pattern for DIC. To record speckle images, a second high speed camera (Phantom SpeedSense, Vision Research), identical to the PIV camera, was installed above the drop tower, pointing vertically downward. A 120W LED light (Constellation 120E, Veritas) was utilized as the light source for DIC. To mitigate potential light interference with PIV, both the DIC camera and LED light source were fitted with red cut-on filters (with a cut-on wavelength of 570 nm for the camera and a cut-on wavelength of 590 nm for the LED light). The DIC camera had a resolution of 1632 \times 1200 pixels and a field of view of around 34.0 \times 25.0 cm. Its focal distance was around 0.90 m, and the aperture of the lens was set to an f-number of 9.6. Similar to the PIV acquisition, we record only the speckle pattern on the right half of the plate. The

DIC camera was set to acquire images at a rate of 1000 Hz with an exposure time of 500 μs . The acquisition of both the PIV and DIC cameras were controlled via the timer box.

In addition to experimental trials on the water-backed plate, we conducted experimental trials in the absence of the water, to help tease out the influence of the fluid–structure interaction on the structural response. During the trials on the air-backed plate, the PIV laser was re-positioned to illuminate the front edge of the plate, and the PIV camera was re-focused on the adjusted illumination plane, providing a side-view of the plate deformation. The side view recording was used to obtain a direct, independent measurement of the deflection of the plate to benchmark the accuracy of DIC.

To facilitate the estimation of the impact force, three accelerometers with different measurement range and sensitivity were installed in a sealed box attached to the impactor: $\pm 3 \text{ g}$ (300 mV/g; Analog Devices, model ADXL335), $\pm 20 \text{ g}$ (100 mV/g; Measurement Specialties, model 805M1), and $\pm 200 \text{ g}$ (10 mV/g; Measurement Specialties, model 805M1). The vertical position of the impactor was also measured via a linear position sensor (Spectra Symbol, TSP-L-0750-203-3%-RH) mounted on the vertical rail. All the accelerometers and the position sensor were powered via a 3 V DC voltage. From our experimental trials, we observed occasional saturation of the $\pm 3 \text{ g}$ accelerometer during the impact, while the $\pm 20 \text{ g}$ accelerometer never saturated during all trials. To ensure an adequate measurement range and a sufficient measurement resolution, we used the readings of the $\pm 20 \text{ g}$ accelerometer to study the dynamics of the impactor.

The hydrodynamic loading on the plate was measured via an injection control pressure (ICP) sensor (PCB Piezotronics, model 113B27) installed on the plate. To avoid blocking of the speckle pattern used in the DIC measurements, the sensor was installed on the left side of the plate, at approximately 1.5 cm from the mid-span. The pressure sensor was connected to a signal conditioner (PCB Piezotronics, model 482C05), which supplied a constant current input. In our trials, all the sensor readings were recorded through a data acquisition (DAQ) board (National Instrument; model USB-6341) at a rate of 4000 Hz for each channel, for a total of five output channels.

The simultaneous control of the instruments and the process of data acquisition are illustrated in Fig. 1(b). At the start of each experimental trial, the DAQ board enabled an Arduino Uno microcontroller to send a high voltage pulse (5 V with a pulse duration of 0.3 s) to both the electromagnet and the timer box input, while simultaneously starting

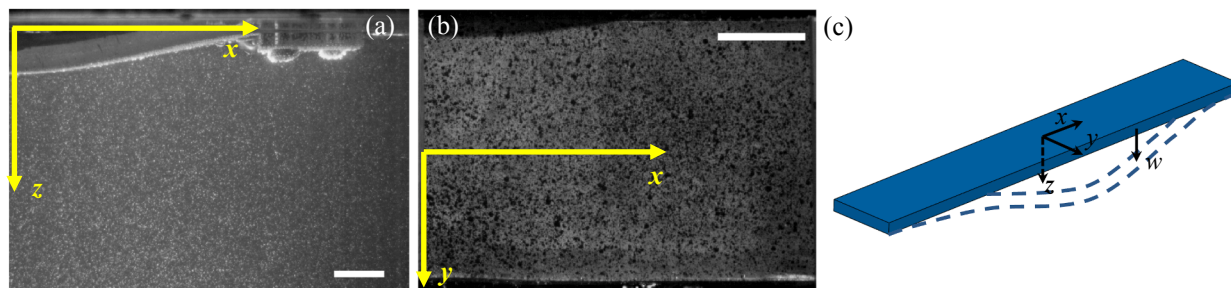


Fig. 2. (a) Exemplary particle and (b) speckle pattern images simultaneously acquired by the PIV and DIC cameras during impact, capturing the deformation of half of the plate and fluid flow of the water below. A coordinate system is defined such that the center of the plate is at the origin. The white bars are 2 cm long. (c) Illustration of the out-of-plane deflection. Dashed curves indicate the deformed shape of the plate.

the recording of the sensors data. The high voltage pulse triggered the acquisition of the cameras through the timer box. At the same time, the high voltage pulse initiated the release of the impactor through a PCB relay (Tyco Electronics; OMI-SH-105L), connected to the power supply of the electromagnet. Images acquired by both the cameras were transferred to a computer hard drive through a router. To assess the repeatability of our experiments, for each test condition we conducted the measurement three times.

Exemplary PIV and DIC images simultaneously acquired during a trial are shown in Fig. 2. Therein, we also indicate the Cartesian coordinate system used in our analysis. The origin of the coordinate system corresponds to the geometric center of the top surface of the plate in its undeformed configuration. The x -axis runs along the length of the plate, the y -axis is along the width of the plate, and the z -axis is along the depth of the tank.

3. Analysis methods

3.1. Structural response of the plate

Given the geometry of the setup and the aspect ratio of the plate, it is tenable to hypothesize that the plate undergoes cylindrical bending and that through-the-thickness deformations are secondary. As a result, the entire structural response is encapsulated by the deflection of the mid-plane of the plate (or any parallel plane), which is independent of the y coordinate. We indicate this deflection field as $w(x, t)$ where t is time, with $t = 0$ being the onset of the impact. DIC-based inference of $w(x, t)$ was comprised of two steps. First, we quantified “apparent” in-plane displacement of the top surface of the plate, $\bar{v}(x, y, t)$, caused by $w(x, t)$ through DIC analysis of the speckle images, see Fig. 2(c). DIC analysis was performed in the open source software, Ncorr [40], implementing a subset-based DIC algorithm. The speckle pattern prior to the impact was used as the reference image, and the deformed speckle images were correlated with the reference image to obtain the apparent in-plane displacement. In the analysis, each speckle image was divided into small subsets, in which the deformation was estimated. A subset radius of 30 pixels and a subset spacing of 3 pixels were utilized in our analysis.

The time-resolved deflection of the plate was then reconstructed from $\bar{v}(x, y, t)$, by implementing the algorithm proposed in [33]. The algorithm is based on a linearized pin-hole camera model, where the focal distance of the camera is assumed to be much larger than the out-of-plane displacement and the image distortion caused by the camera lens is neglected. Such a model was applicable in our setup for the following reasons. First, the plate deflection in our experiment was of the order of 2 cm, which is only 2% of the focal distance (0.90 m). Second, the large f-number of the DIC camera lens ensured that the depth of field was sufficiently large, such that the speckle pattern remained in focus during the entire impact. Finally, no distortion of the images acquired by the camera was observed. Alternatively, one could

opt for the use of multiple cameras as in [25], but this would require increased data storage and processing, as well as a more intricate experimental implementation.

The linearized pin-hole camera model is briefly described below. Under the assumption that the plate undergoes no translational rigid body motion, we can express the out-of-plane displacement $w(x)$ as a function of the in-plane displacement along the y -direction as [33]

$$\bar{v}(x, y, t) \approx kyw(x, t), \quad (1)$$

where the proportionality constant k is related to the camera magnification factor, M , and the distance between the lens and the image plane of the camera, q . This relationship is exact if the apparent in-plane displacement depends linearly on y , which would be the case if the plate precisely underwent cylindrical bending. To account for experimental uncertainty and potential in-plane deformation, we chose to satisfy this relationship in an average sense, as follows:

$$w(x, t) = \frac{1}{k} \left\langle \frac{\partial \bar{v}(x, y, t)}{\partial y} \right\rangle, \quad (2)$$

where $\langle \cdot \rangle$ means averaging from $-b/2$ to $b/2$. The slope of the apparent displacement, $\partial \bar{v}(x, y, t)/\partial y$, was obtained through numerical differentiation of $\bar{v}(x, y, t)$ via a central difference scheme, using a uniform grid along the y -axis with spacing of 0.83 mm.

In principle, $w(x, t)$ can also be related to the apparent in-plane displacement along the x -direction. However, the relation between these quantities is not as straightforward as Eq. (1). In addition to the apparent in-plane strain associated with deflection, the surface strain along the x -direction resulting from the bending of the plate will also act as an experimental confound.

The value of the unknown constant k was determined from a static calibration test conducted using the same DIC camera setup prior to the experiments. We obtained the value of k through the linear correlation between a series of $\langle \partial \bar{v}(x, y, t)/\partial y \rangle$ measured through DIC with the independent measurement of the deflection of the plate, $w(x, t)$. A series of weights, with a mass ranging from 8.6 to 732 g, were applied at the mid-span of the plate. The speckle pattern was recorded by the DIC camera for each load, which was used to compute the value of $\langle \partial \bar{v}(x, y, t)/\partial y \rangle$ in Eq. (2). The deflection of the plate was independently measured from image analysis of the side-view PIV camera, which recorded the plate shape for each loading condition. The value of k in Eq. (2) was then estimated through a linear fit between $\langle \partial \bar{v}(x = 0, y, t)/\partial y \rangle$ and $w(x, t)$.

Theoretically, the value of k is constant if the plate surface in its reference configuration is perfectly perpendicular to the optical axis of the DIC camera. However, in our experiment, the plate was bent due to gravity, causing its top surface to be misaligned with respect to the focal plane. Consequently, using the same k value at all the x locations would introduce error in the estimation of the out-of-plane displacement of the plate [33]. To mitigate this issue, we calibrated a sequence of values of k on 107 equally spaced grid points from the mid-span to the clamp of

the plate. The reconstruction of the deflection at a specific value of x was then conducted based on the calibration constant k obtained at the nearest location.

The side view images recorded during dry impact were utilized to benchmark the DIC measurement. The images were processed using a custom-developed image analysis program built in MATLAB. Each image was first transformed into a binary image, with the bright side view of the plate converted to white and the dark background to black. The vertical position of the mid-span was then identified by searching the first white pixel along the central column of the image, and its position was used to generate a time-history of the mid-span deflection. Image tracking can afford pixel-level accuracy in the estimation of the plate deflection during dry impact. In principle, the approach could be extended to the study of water-backed impact, where images of the plate deflection are available from PIV recordings. However, the fact that the depth-of-field of the PIV camera is smaller than the width of the plate causes the front edge of the plate on the foreground to be blurry, thereby challenging the accuracy of the measurement of the plate deflection. Light distortions due to water splash, surface waves, and air ventilation during impact could introduce further uncertainty in the tracking of the plate deflection. All these sources of uncertainty are mitigated by using DIC on images from the top-view camera.

3.2. Flow physics

The two-dimensional fluid velocity field, $\mathbf{u}(x, z, t)$, during impact was obtained from the particle images through the open source PIV analysis software, PIVlab [41]. Briefly, the plate and clamp were first manually masked from each particle image. Consecutive images were then cross-correlated using a fast Fourier transform algorithm. Cross-correlation was conducted on three levels of interrogation windows, from 64×64 to 32×32 to 16×16 pixels, with a 50% window overlap.

The hydrodynamic pressure field, p , was then reconstructed from the velocity field using a Poisson equation-based approach [30,31]. From the incompressible Navier-Stokes equations,

$$\nabla p(x, z, t) = -\rho \left(\frac{\partial \mathbf{u}(x, z, t)}{\partial t} + \mathbf{u}(x, z, t) \cdot \nabla \mathbf{u}(x, z, t) \right) + \mu \nabla^2 \mathbf{u}(x, z, t) + \rho g, \quad (3a)$$

$$\nabla \cdot \mathbf{u}(x, z, t) = 0, \quad (3b)$$

with g being gravity along the z -axis, we obtain the Poisson equation for the pressure field

$$\nabla^2 p(x, z, t) = -\rho S(x, z, t), \quad (4)$$

where $S(x, z, t) = \nabla \cdot (\mathbf{u}(x, z, t) \cdot \nabla \mathbf{u}(x, z, t))$ is the source term, which can be evaluated directly from the velocity field numerically using a central difference scheme. To solve for the unknown pressure field, we first mirrored the measured fluid velocity field to construct the entire fluid domain below the plate, as illustrated in Fig. 3. Eq. (4) was then discretized using a five-point central difference scheme. As sketched in Fig. 3, we use subscript i and j to identify the grid points along the x - and z -directions in the velocity field obtained from PIV. The pressure at a point in the fluid domain was related to its neighboring points by

$$p_{i,j+1}(t) + p_{i,j-1}(t) - 4p_{i,j}(t) + p_{i+1,j}(t) + p_{i-1,j}(t) = -\rho \delta S_{i,j}(t), \quad (5)$$

where δ is the spacing between neighboring grid points along the x - or z -axes, and we use subscript to identify grid points as shown in Fig. 3.

On the boundary of the region of interest, we imposed a mixed Dirichlet and Neumann boundary condition. We applied the Dirichlet boundary condition for pressure on boundaries Γ_L , Γ_B , and Γ_R of the region of interest as well as on the free surface Γ_{SL} and Γ_{SR} . The pressure values at these boundaries were obtained from direct integration of Eq. (3a) along the boundary. A point on the free surface, "A", was chosen as a reference point with null pressure for all times.

Along the plate-water (Γ_P) and the clamp-water (Γ_{CL} and Γ_{CR})

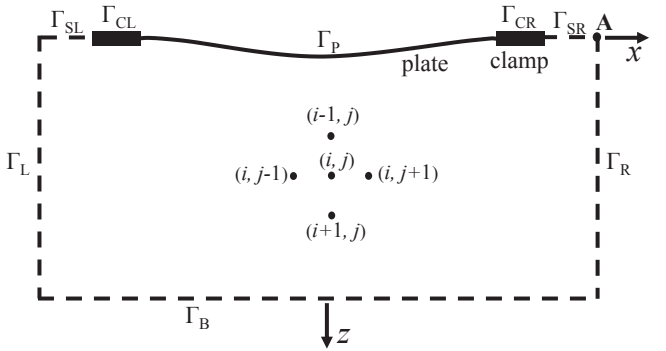


Fig. 3. Schematic of the Poisson equation-based pressure reconstruction, including an illustration of the five point central difference scheme and definitions of the boundaries of the region of interest.

interfaces, we imposed the Neumann boundary condition for pressure, whereby the value of $\partial p(x, z, t)/\partial n$ was treated as a known input, with n being the outward normal. The value of $\partial p(x, z, t)/\partial n$ at the plate-water interface was computed from Eq. (3a) using the measured velocity field from PIV. Ghost points outside of the region of interest were used to enforce the Neumann boundary condition for the pressure. Pressure values at the ghost points were linearly extrapolated from the pressure inside the region of interest. To simplify the numerical implementation of the Neumann boundary condition, the normal direction to the plate was assumed to be always along the z -direction. The pressure reconstruction algorithm was performed marching in time, until we observed air ventilation under the plate.

4. Results

Here, we present our main results on the simultaneous quantification of the structural response and the fluid flow elicited by the impact. First, the accuracy of the DIC-reconstructed plate deflection is benchmarked through comparison with image tracking of the mid-span deflection and direct reading from the impactor position, for air-backed impact. DIC is then employed to study the influence of the water on the dynamics of the plate, by critically comparing the severity and time scale of the plate deflection in water-backed and air-backed impact. From the measured deflection, we garner important insight into the structural response, through the computation of the elastic energy associated with bending and membrane stretching, whose interplay define the nonlinearity in the impact response. With an eye toward collecting experimental evidence that can help validating existing mathematical models, we also undertake modal analysis to assess the extent by which the response can be described by using a single mode shape (fundamental in-vacuum mode shape of the plate), as commonly proposed in the literature [15–17].

We then focus on the flow physics associated with water-backed impact. Similar to DIC analysis, we first seek to validate PIV measurements through comparison with independent dataset. Toward this aim, we compare the fluid velocity at the mid-span of the plate with the sensors measurements of the impactor velocity, inferred from accelerometer data. To assess the accuracy of the reconstructed pressure field, we compare PIV measurement with pressure sensor data at the location of the sensor. Similar to DIC, we also attempt at a modal analysis of the pressure field, by quantifying the contribution of the hydrodynamic loading on the fundamental in-vacuum mode shape of the plate.

To ease the presentation of our results, we introduce a characteristic time scale based on the fundamental in-vacuum vibration period of the plate, defined as $T = 1/\omega_1$, where $\omega_1 = \frac{\lambda_1^2 h}{L^2} \sqrt{\frac{E}{12\rho_b}}$, with $\lambda_1 = 2.365$. We also introduce the associated characteristic pressure as $P = \rho h^2 \omega_1^2$. For the selected physical parameters, $T = 14.3$ ms and $P = 486.9$ Pa. Also,

Table 1

A list of physical and geometric parameters.

Property	Symbol	Value
Plate half-length	L	9.5 cm
Plate thickness	h	1.0 cm
Plate width	b	6.0 cm
Impactor drop height	H	1–10 cm
Impactor mass	M	231.7 g
Effective Young's modulus	E	1.58 MPa
Plate mass density	ρ_b	1.02×10^3 kg/m ³
Water density	ρ	1.00×10^3 kg/m ³
Characteristic time scale	T	14.3 ms
Characteristic pressure	P	486.9 Pa
Nominal impact velocity	v_0	0.44–1.40 m/s

when presenting flow field results, we scale the fluid velocity by the estimated velocity of the impactor, $v_0 = \sqrt{2gH}$. A list of all the parameters and characteristic values for the nondimensionalization is reported in Table 1.

4.1. Validation of DIC measurements

The accuracy of the DIC measurement was evaluated through comparison with image tracking of the mid-span deflection of the plate from the side-view camera during air-backed impact, as shown in Fig. 4. For all the drop heights, we find that the deflection reconstructed from DIC was in good agreement with image tracking, especially for moderate deformation. For $H = 1$ cm, the maximum difference between image tracking and DIC is around $0.14h$. For larger drop heights, as the deflection increases over time, the discrepancy between image tracking and DIC becomes more notable. For $H = 10$ cm, the maximum difference can be as high as $0.39h$. In addition to point-wise comparison, we assessed the accuracy of DIC in full-field measurement of the plate deflection against image tracking. The maximum difference in the plate deflection between DIC and image tracking is $0.25h$ for drop height $H = 1$ cm and $0.66h$ for drop height $H = 10$ cm, which are of the same

order of magnitude of data at the mid-span of the plate.

The more significant discrepancies, registered for the largest drop height, might be attributed to variations in the magnification of the camera during the impact response. In fact, calibration of the out-of-plane reconstruction process, detailed in Section 3.1, was conducted under the premise that the magnification of the camera would remain constant as the speckle pattern experienced the out-of-plane displacement. However, this is true only for small deflections, whereby for deflections larger than 2 cm, it is possible that the camera magnification sensibly changed during the impact. A growing error in DIC for increasing out-of-plane displacements has also been previously reported [33]. Localized deformations and higher order modes triggered by large drop heights could also have contributed to the discrepancy between DIC and image tracking during the initial stage of the impact.

In most practical applications [2,42,43], the motion of the impactor is used for estimating the plate deflection, which should be accurate for small through-the-thickness deformation of the plate and continuous contact between the plate and the impact. Comparison of the vertical motion of the impactor, acquired through the position sensor, with DIC and image-tracking results on the mid-span deflection of the plate in Fig. 4 supports the use of the impactor motion as a proxy for the plate deformation at its mid-span. However, such a measurement does not offer insight into the overall deformation of the plate, which is instead possible by using cameras for DIC or image tracking. Also, a larger variability is noted with respect to the other approaches, which might be ascribed to uncertainty in the contact between the plate and the impactor across repetitions.

4.2. DIC-based quantification of the structural response of the plate

The DIC-based mid-span deflections for water- and air-backed impact are shown in Fig. 5. Predictably, the water-backed plate deformed at a slower time scale, due to the added mass effect [6,11,17,44]. Within a first degree of approximation, water-backing can be associated with an additional mass, proportional to the wetted surface of the plate, which will be displaced during the impact. As a result, the impact should be slower for water-backing than air-backing.

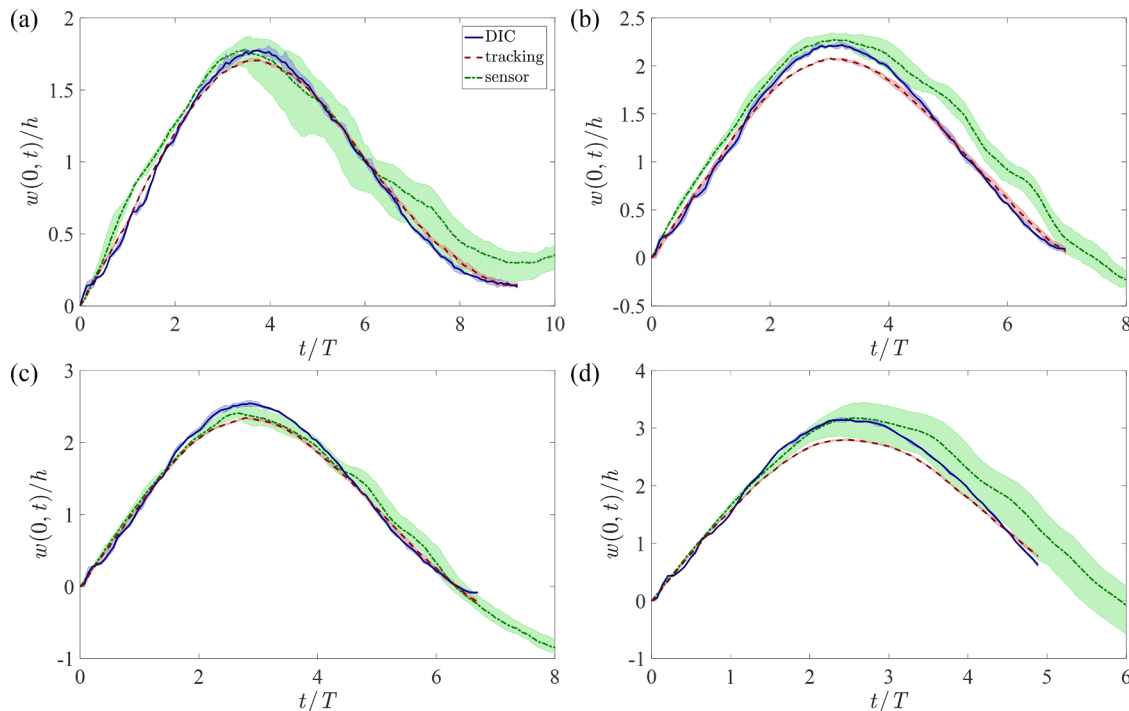


Fig. 4. Time-histories of the plate mid-span deflection for air-backed impact, measured through DIC, image tracking, and position sensor for drop heights: (a) $H = 1$ cm, (b) $H = 3$ cm, (c) $H = 5$ cm, and (d) $H = 10$ cm. The shaded areas are lower and upper bounds, based on three repetitions, and lines represent mean values.

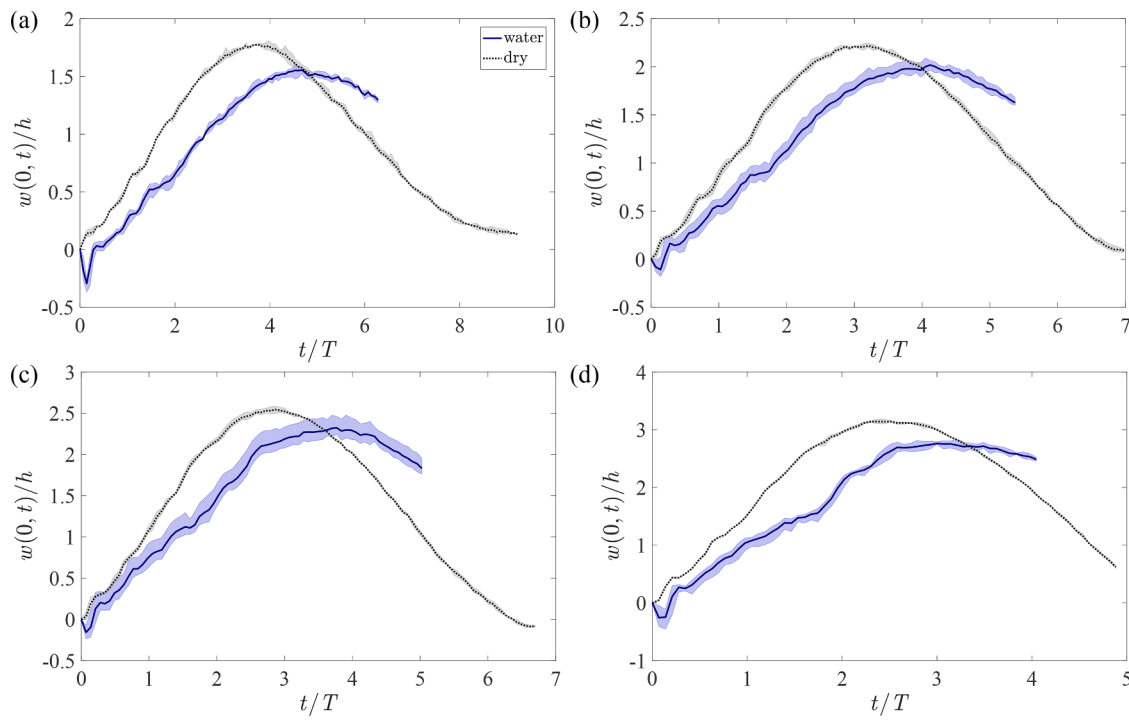


Fig. 5. Mid-span deflection of the plate under water-backed and air-backed impact measured by DIC for drop heights: (a) $H = 1\text{ cm}$, (b) $H = 3\text{ cm}$, (c) $H = 5\text{ cm}$, and (d) $H = 10\text{ cm}$. The shaded areas are lower and upper bounds, based on three repetitions, and lines represent mean values. Note that the initial upward deflection in DIC was likely an artifact caused by imperfect contact between the impactor and the plate at the onset of the impact. The effect of this imperfection became negligible after the impactor made full contact with the plate.

With respect to the magnitude of the peak displacement, the water-backed plate experienced a smaller deformation, which is in agreement with [11], but in contrast with [2]. Perhaps, the unexpected finding in [2] is due to the damage of the material during impact. As detailed in [8], water-backed impact elicits larger contact forces, which may cause local damage. For small impact velocities, even if the load is larger, the presence of added mass causes a reduction in the deformation, but for higher velocities, the onset of damage could ultimately lead to higher deformation.

To better illustrate the interplay between the severity of the deformation and its time scale, in Fig. 6, we compared the maximum deflection, w_{\max} , and the time at which it is attained, t_{\max} , for water- and air-backed impact. In agreement with our expectations, w_{\max} decreases

with t_{\max} , such that slower dynamics will lead to less severe deformation. For a given value of t_{\max} , the deflection for water-backed impact seems slightly larger than the corresponding value for the air-backed case, although, to a first degree of approximation, one may propose a common dependence on the time-scale of the impact. Specifically, a linear regression of the entire dataset explains 91% of the experimental variation: $w_{\max}/h = -0.68t_{\max}/T + 4.64$ ($R^2 = 0.91$, $p < 0.01$). Faster time-scales correspond to larger impact velocity, which trigger membrane-stretching of the plate, thereby contributing to increased stiffness for a comparable inertia [44].

Elucidating the interplay between linear and nonlinear phenomena during impact can be undertaken by studying the deflection profiles of the plate for water- and air-backing. While the measurements in Fig. 5 could in principle be acquired from the motion of the impactor, comparing the deflection profiles of water-backed and air-backed plates requires distributed measurements, which are afforded by DIC. The profiles of the plate deflection reconstructed from DIC are displayed in Fig. 7 at various time instants for both water- and air-backed impact for the smallest ($H = 1\text{ cm}$) and the largest ($H = 10\text{ cm}$) drop heights. Independent of the drop height and the impact condition, the maximum deflection was consistently located around the mid-span. In general, the deflection profiles seemed to follow at all times the fundamental invacuum mode shape given by

$$m(x) = m_0 \left(\cos(\lambda_i x/L) - \frac{\cos(\lambda_i)}{\cosh(\lambda_i)} \cosh(\lambda_i x/L) \right), \quad (6)$$

where $m_0 = 3.208$, such that $\int_{-L}^L (m(x))^2 dx = 1$. However, some qualitative differences can be noted when comparing water- versus air-backing as well as the two drop heights.

First, in the early state of the impact, the deflection for water-backing seems to contain higher mode shapes, which are less evident during air-backed impact. To quantitatively support this observation, we computed the modal contribution factor

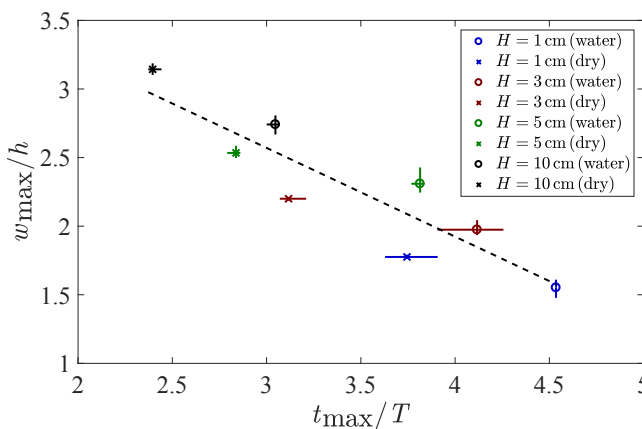


Fig. 6. Maximum deflection (w_{\max}) and the time at which it is attained (t_{\max}) for water-backed and air-backed impact for all drop heights. The vertical and horizontal error bars represent lower and upper bounds obtained from three repetitions of w_{\max}/h and t_{\max}/T , respectively. The black dashed line is a linear regression of the entire dataset.

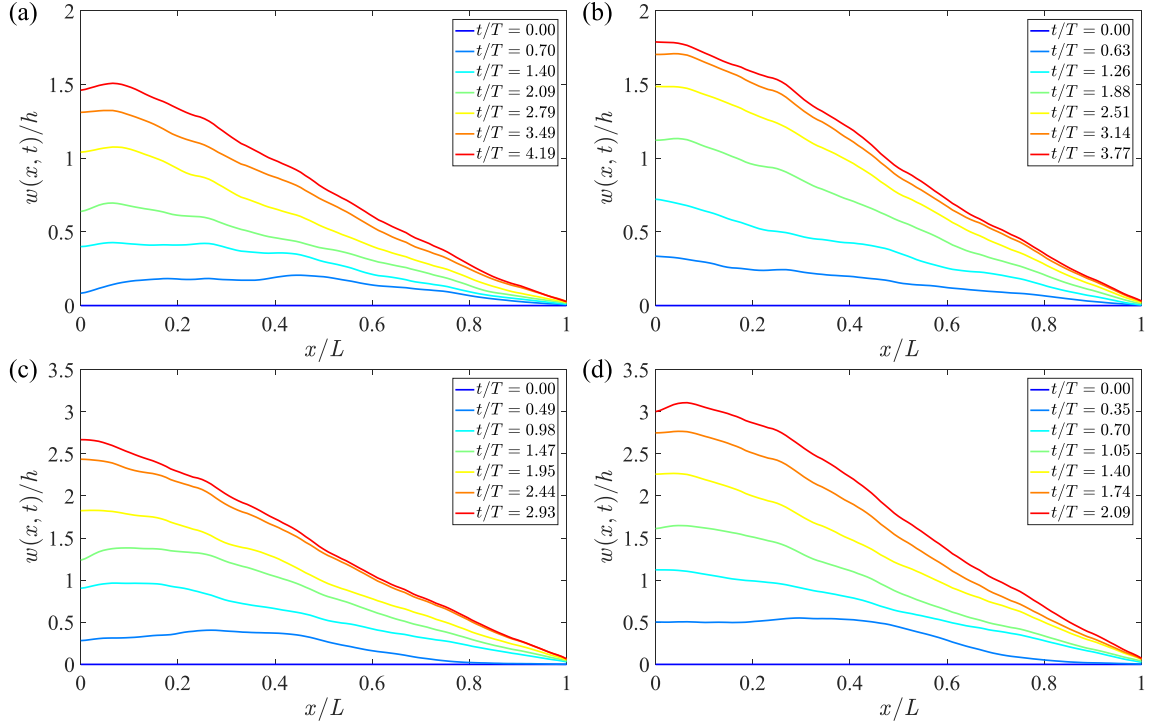


Fig. 7. Time-histories of the deflection profiles estimated through DIC for drop height (a,b) $H = 1 \text{ cm}$ and (c,d) $H = 10 \text{ cm}$ under (a, c) water- and (b, d) air-backed impact. Seven equally-spaced time instants between 0 and t_{\max} are selected for each panel. Results refer to one of the three trials.

$$w_1(t) = \frac{\sqrt{2} \left| \int_0^L w(x, t) m(x) dx \right|}{\sqrt{\int_0^L (w(x, t))^2 dx}}, \quad (7)$$

such that $0 \leq w_1(t) \leq 1$. $w_1 = 1$ indicates that the plate deflection is closely represented by the fundamental in-vacuum mode shape, while a small value of w_1 suggests that other mode shapes better explain the impact. As shown in Fig. 8(a), the value of w_1 started from low values between 0.20 and 0.65 at the onset of the impact, before reaching a value close to 1 at approximately $t/T = 1$. In contrast, during air-backed impact, the plate quickly reached a modal contribution factor 1, as shown in Fig. 8(b).

Second, as more severe deformations were attained for the largest drop height, the overall plate deflection resembled a “wedge-like” profile, similar to the static deflection of a rope under a concentrated load. This phenomenon should be related to membrane-stretching dominating bending stiffness, such that the plate will deform similar to a membrane as the deflection becomes larger than the thickness. To support this claim, we estimated the bending energy and the stretching

energy stored in the plate from the deflection, defined by [45]

$$U_b(t) = \frac{Ebh^3}{12} \int_0^L \left(\frac{\partial^2 w(x, t)}{\partial x^2} \right)^2 dx, \quad (8a)$$

$$U_s(t) = \frac{Ebh}{4} \int_0^L \left(\frac{\partial w(x, t)}{\partial x} \right)^4 dx. \quad (8b)$$

The ratio of the bending energy over the total strain energy ($U(t) = U_b(t) + U_s(t)$) is displayed in Fig. 9 as a function of time. For both water- and air-backed impact, deformation of the plate was dominated by bending at the initial stage of the impact, when the deflection is small. Predictably, membrane-stretching became more prominent as the deflection increases over time, especially for the largest drop height where it could account for almost 80% of the total strain energy. Comparing water- and air-backed impact for the smallest drop height ($H = 1 \text{ cm}$), we note that the presence of water significantly reduces the severity of membrane stretching, while no reduction is observed for the largest drop height ($H = 10 \text{ cm}$).

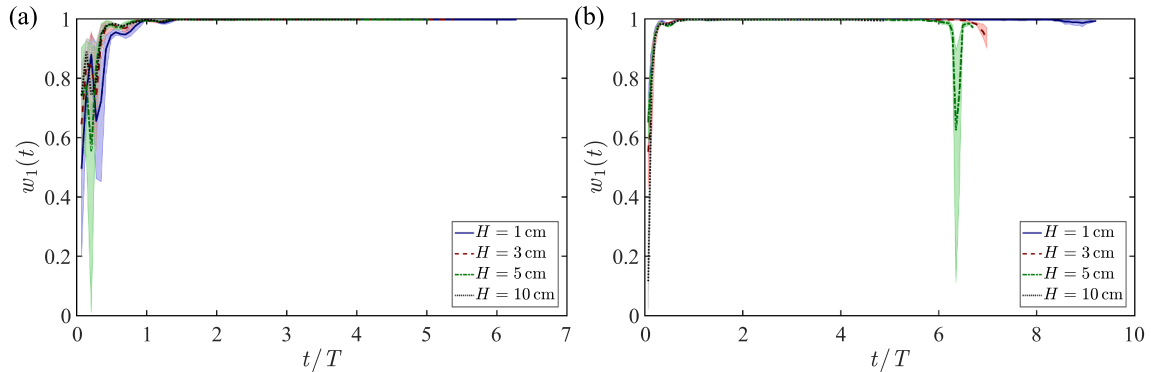


Fig. 8. Time-histories of the plate deflection projected on the fundamental in-vacuum mode shape $m(x)$ for (a) water- and (b) air-backed impact for all drop heights. The shaded areas are lower and upper bounds, based on three repetitions, and lines represent mean values. The outlier for $H = 5 \text{ cm}$ at $t/T \approx 6.5$, corresponding to the time instant when the plate returns to its undeformed shape, is likely a result of measurement noise, where it is just found in one of three repetitions.

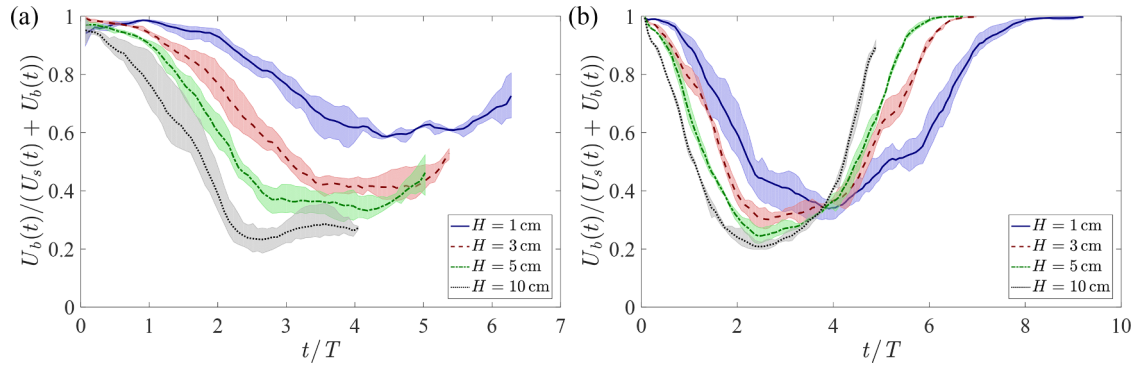


Fig. 9. Ratio between the bending energy and the total strain energy stored in the plate, as a function of time for (a) water- and (b) air-backed impact at all drop heights. The shaded areas are lower and upper bounds, based on three repetitions, and lines represent mean values. Note that the graph on the left is from $t/T = 0$ to 7, while on the right we plot from 0 to 10.

4.3. Validation of PIV measurements

To shed light on the flow physics during the impact, the velocity field was analyzed through PIV for all drop heights. As a result of the air ventilation observed for the impacts at large drop heights, we had to terminate our PIV analysis for $H = 5\text{ cm}$ and $H = 10\text{ cm}$ at much earlier times than $H = 1\text{ cm}$ and $H = 3\text{ cm}$. No air ventilation was registered for $H = 1\text{ cm}$ and $H = 3\text{ cm}$, and the PIV analysis was conducted for a full cycle of the plate vibration.

PIV measurement at the mid-span of the plate was first validated through sensor recordings and image tracking. The fluid velocity measured by PIV was compared with the recorded velocity of the impactor, as well as with the velocity of the plate at the mid-span. The plate velocity was computed by numerically differentiating its position, manually identified from the PIV images, using a central difference scheme. The velocity of the impactor was obtained by integration of the accelerometer data. Fig. 10 shows a comparison between these independent measurements. We found good agreement between the velocity estimations from the accelerometer and the tracked position of

the plate, confirming that the impactor was in contact with the plate and that through-the-thickness deformations were secondary. However, PIV tended to underestimate the fluid velocity, especially during the initial stage following the impact. This could be attributed to the interrogation windows used for PIV analysis, which only produced a spatial averaged velocity value within each interrogation window. Such a spatial averaging would fail to capture the large velocity gradient below the mid-span of the plate, as also discussed in our previous work on water-entry problems [29,39].

The hydrodynamic loading on the plate was extracted from the two-dimensional reconstructed pressure field on the plate bottom surface. The PIV-based reconstructed pressure is compared with the sensor measurement in Fig. 11. The hydrodynamic loading estimated through PIV tended to underestimate the magnitude of the initial peak in the pressure. This again could be attributed to limitations of PIV in accurately resolving local values of the velocity field, especially at the onset of the impact when the velocity gradient is large, as discussed in [29,39]. However, PIV successfully captured the onset of the impact and provided an order-of-magnitude estimation of the pressure at the

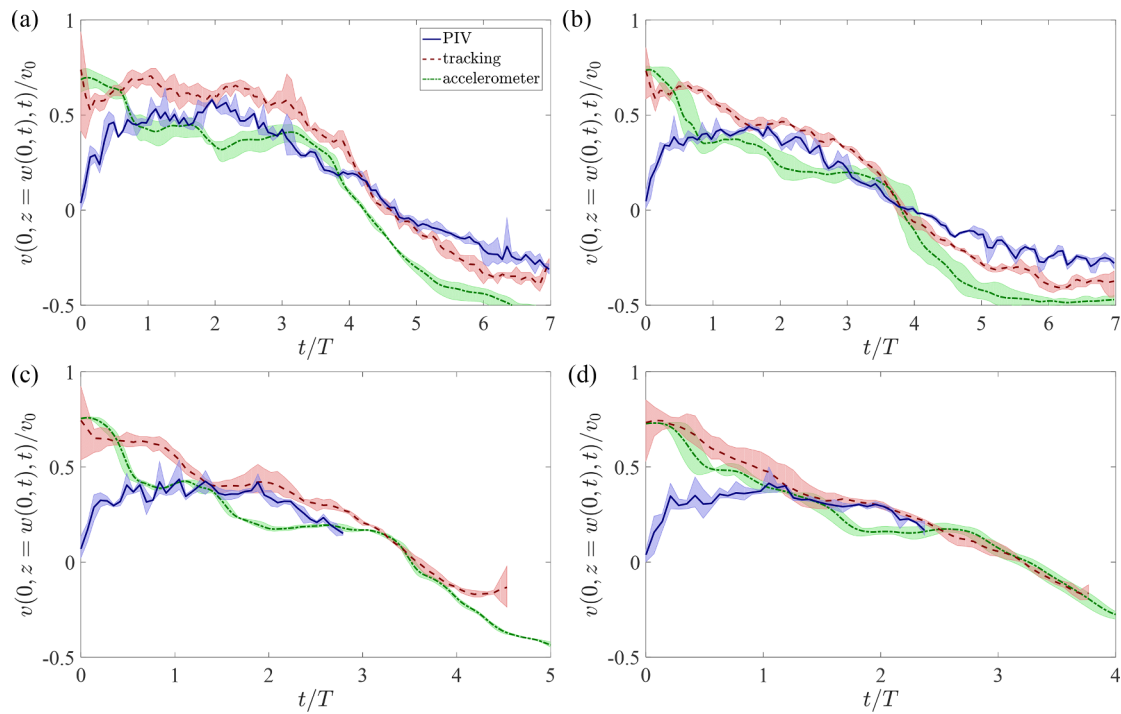


Fig. 10. Vertical velocity at the plate mid-span measured through the accelerometer, image tracking, and PIV for drop heights: (a) $H = 1\text{ cm}$, (b) $H = 3\text{ cm}$, (c) $H = 5\text{ cm}$, and (d) $H = 10\text{ cm}$. The shaded areas are lower and upper bounds, based on three repetitions, and lines represent mean values.

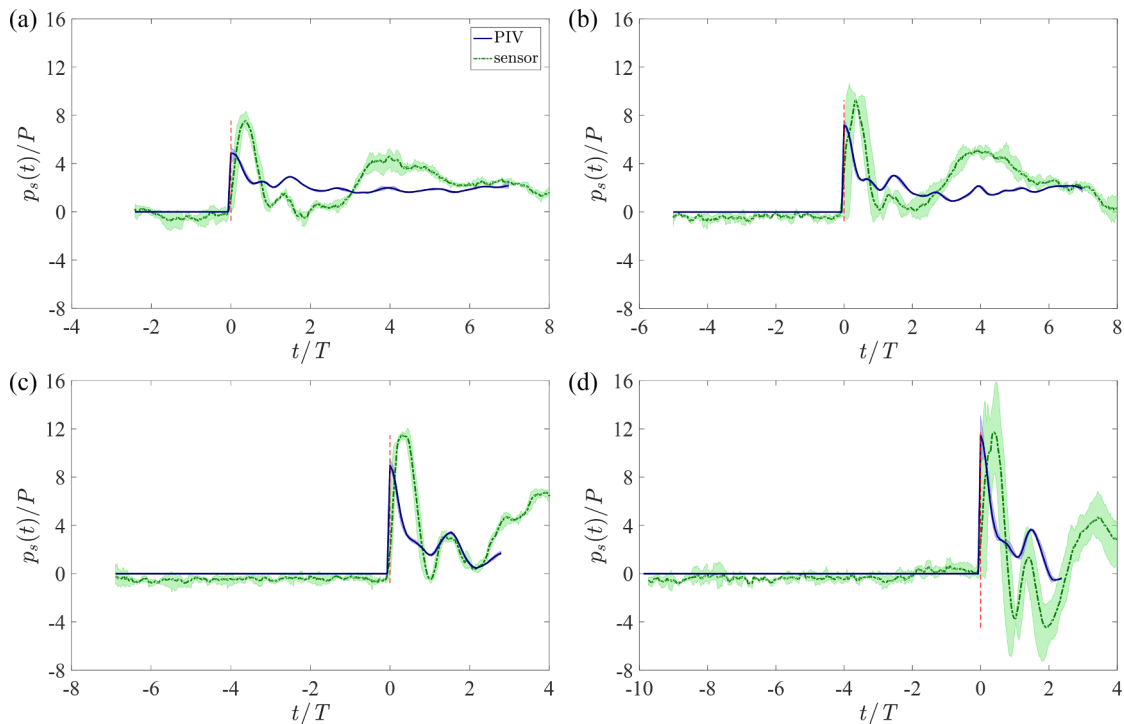


Fig. 11. PIV-based pressure reconstruction and direct sensor measurement at the location of the pressure sensor on the plate for drop heights: (a) $H = 1$ cm, (b) $H = 3$ cm, (c) $H = 5$ cm, and (d) $H = 10$ cm. Here, $p_s(t)$ is the pressure at the location of the pressure sensor, $p_s(t) = p(x = 0.16L, z = w(x = 0.16L, t), t)$. The shaded areas are lower and upper bounds, based on three repetitions, and lines represent mean values. The red dashed vertical lines indicate $t = 0$.

location of the pressure sensor. Given experimental challenges in conducting the direct measurement with pressure sensors and the related experimental uncertainty, it should not to be excluded that PIV readings are closer to the true pressure than the reading of the sensor.

4.4. Flow physics

To shed light on the flow physics during impact, we examined the velocity and pressure field below the plate as a function of time. The planar distribution of the velocity field for the lowest ($H = 1$ cm) and the largest ($H = 10$ cm) drop heights is displayed in Fig. 12 at two time instants, representative of the onset of the impact and the later stage when the plate undergoes large deformation. Specifically, we considered $t = 0.1t_{\max}$ and $t = t_{\max}$ – due to air ventilation at the largest drop height, we could only acquire PIV leading up to $t/T = 2.37$, which was less than $t_{\max}/T = 3.07$. For both the drop heights, a high velocity region can be observed below the mid-span of the plate, shortly after the impact (Fig. 12(a) and (b)), due to the localized velocity imparted to the plate by the impactor. As the plate attained its maximum deflection, the velocity magnitude became significantly smaller (Fig. 12(c) and (d)).

The pressure field associated with the velocity fields in Fig. 12 is displayed in Fig. 13. At $t = 0.1t_{\max}$, the pressure field featured a high pressure region below the mid-span of the plate. The high pressure region was possibly due to the sudden acceleration of the plate, which caused the fluid to accelerate, thereby building up the pressure in the fluid. As the plate approached its maximum deflection in the later stage of the impact, the pressure was significantly reduced, and no apparent peak in the pressure field could be observed. Interestingly, for $H = 10$ cm, a negative pressure (that is, lower than the pressure on the free surface) could be observed in the vicinity of the plate. This negative pressure region was likely associated with the deceleration of the plate, which caused the fluid to also decelerate and virtually pull the plate downward. Air ventilation observed for $H \geq 5$ cm could be partially attributed to the formation of this negative pressure region, which

could facilitate air to advect below the plate. Although the pressure reaches negative values, these values are always in magnitude much larger than the vapor pressure, namely, 500 Pa versus 2 kPa, so that cavitation is not feasible.

To offer some quantification of the fluid-structure interaction, in Fig. 14, we show the profiles of the hydrodynamic loading on the plate at the same time instants considered in Fig. 7 for the deflection of the plate. Different from the deflection profiles, the hydrodynamic loading was not a stationary wave, captured by a single mode shape. More specifically, a localized pressure peak at the mid-span of the plate was identified at the onset of impact. As time progresses, the pressure peak tended to diffuse while shifting from the mid-span to the clamp, before redirecting back, toward the mid-span. Fig. 15(a) illustrates the pressure at the mid-span for all the drop heights, indicating that the pressure peak continued to travel back and forth along the span of the plate for the entire duration of the recording, albeit slowly diffusing. Interestingly, the time-scale associated with the motion of the pressure peak seemed to be on the order of T , independent of the drop height.

Consistent with this analysis, the modal contribution factor for the hydrodynamic loading, defined as in Eq. (7), did not approach one as time progresses, but oscillated with a period of approximately T , as shown in Fig. 15(b). Comparing Fig. 15(b) with Fig. 14, the local maximum of p_1 during each period could be associated with the time when the pressure peak was around the mid-span of the plate, while the local minimum of p_1 corresponds to instances when the pressure peak was near the clamp.

To a first degree of approximation, the added mass effect can be estimated from the ratio between the following quantities:

$$I_{\text{am}} = 2 \int_0^L p(x, 0, t) m(x) dx, \quad (9a)$$

$$I_{\text{dry}} = 2 \int_0^L \rho_b h \frac{\partial^2 w(x, t)}{\partial t^2} m(x) dx, \quad (9b)$$

which encapsulate, respectively, the inertia of the displaced water and the inertia of the dry plate along the fundamental in-vacuum mode

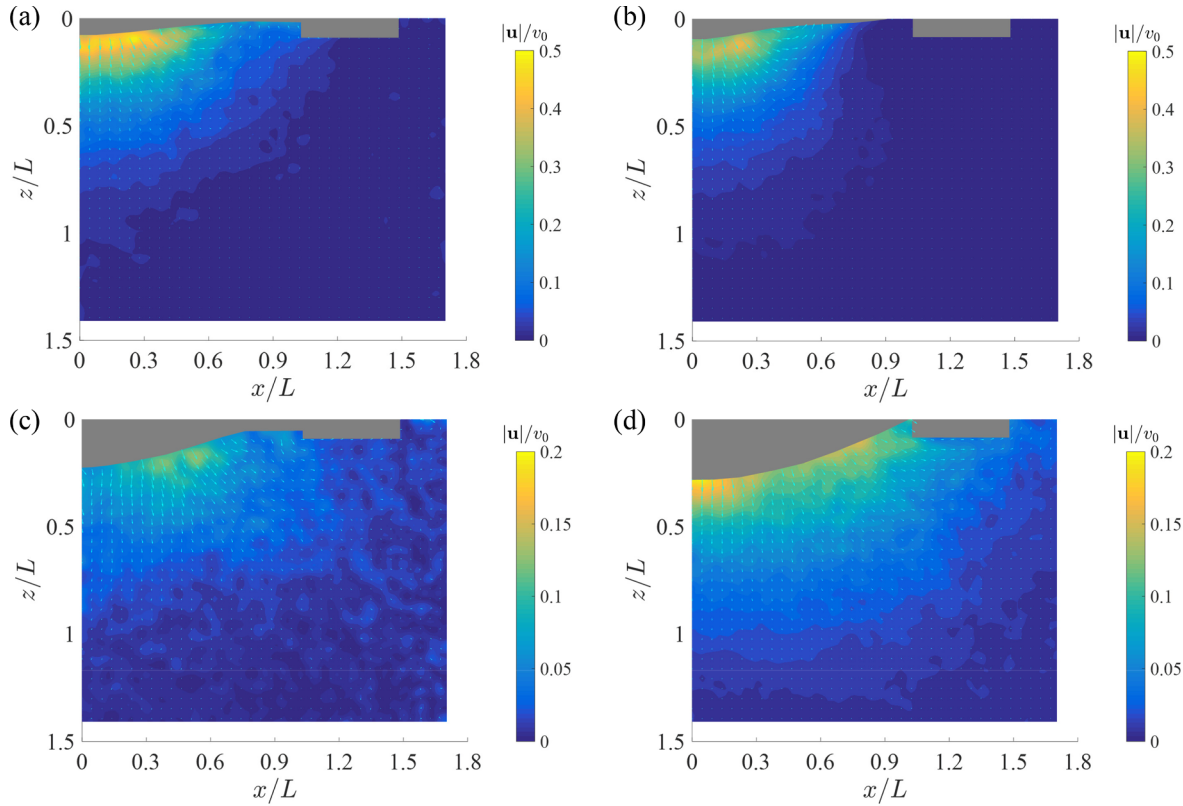


Fig. 12. Velocity field measured by PIV for (a,c) $H = 1 \text{ cm}$ and (b,d) $H = 10 \text{ cm}$. The time instants correspond to (a,b) $t = 0.1t_{\max}$ and (c) $t = t_{\max}$. In (d), the velocity field is shown at the last time instant before the onset of air ventilation, such that the mid-span deflection is $0.89w_{\max}$. Gray areas represent the masks created for the plate and clamp during the PIV analysis. Results refer to one of the three trials.

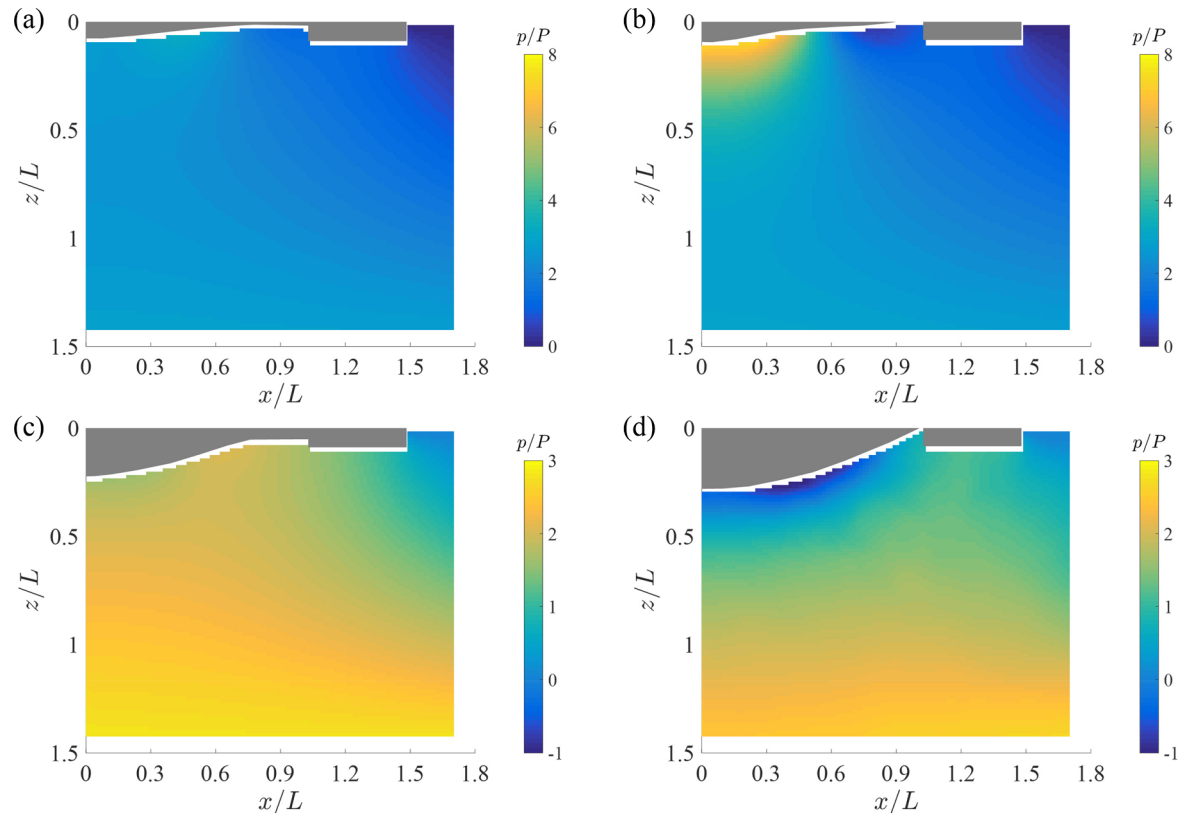


Fig. 13. Pressure field reconstructed from the velocity field for (a,c) $H = 1 \text{ cm}$ and (b,d) $H = 10 \text{ cm}$. The time instants correspond to (a,b) $t = 0.1t_{\max}$, (c) $t = t_{\max}$. In (d), the pressure field is shown at the last time instant before the onset of air ventilation. Gray areas represent the masks for the plate and the clamp. Results refer to one of the three trials.

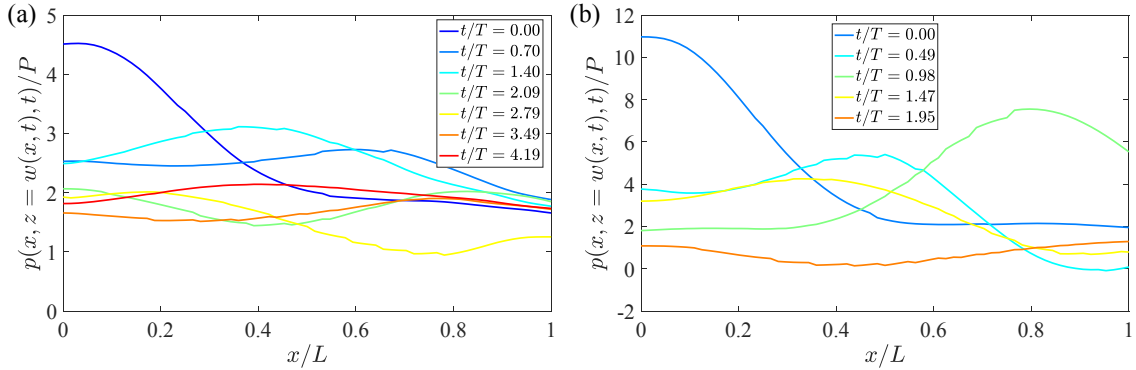


Fig. 14. Profiles of the hydrodynamic loading profiles on the plate for drop heights (a) $H = 1 \text{ cm}$ and (b) $H = 10 \text{ cm}$, at the time instants considered in Fig. 7(a) and (c), respectively. Results refer to one of the three trials.

shape. In our recent work on theoretical modeling of the water-backed impact, we estimated $I_{\text{am}}/I_{\text{dry}}$ to be 7.63 through potential flow theory [15]. Using the hydrodynamic loading reconstructed from PIV and the plate deflection measured by DIC, we experimentally estimated such a ratio to be on average 6.23, which is reasonably close to the theoretical prediction. We should note, however, that this identification is affected by a large uncertainty (with a standard deviation of the order of the mean), due to the need to numerically evaluate second order derivatives in time for the DIC-based deflection as well as inherent-uncertainties in both DIC- and PIV-based inferences.

5. Conclusions

In this work, we proposed a combined experimental technique for the study of low-speed impact on a flexible plate resting on the water surface. Our approach is based on the integration of DIC and PIV, the gold standard experimental techniques for non-invasive analysis of motion in solid and fluid mechanics. DIC was implemented from a top view of the impact to afford the precise reconstruction of the deflection of the plate. PIV was, instead, carried out on a side view of the tank to capture the flow physics in the plane at the middle of the plate width, where three-dimensional effects play a secondary role. Inferences of kinematic and kinetic quantities from DIC and PIV were benchmarked against traditional measurements acquired through the use of accelerometers, position sensors, and pressure sensors. By integrating insight from DIC and PIV, we have attempted at offering a comprehensive analysis of water-backed impact, entailing the structural response of the plate and the concurrent flow physics.

Through the use of DIC, we sought to assess the influence of water backing by comparing the structural response of water- and air-backed plates. Our findings confirm the intuition that the presence of the water causes a reduction in the time-scale of the impact, due to the added

mass phenomenon. We also document a reduction in the severity of the deformation, accompanied by a significant change in the profile of the deflection field. While the response of air-backed plates is accurately captured by using the fundamental in-vacuum mode shape throughout the entire impact, modal analysis suggests that water-backing elicits multiple modes at the onset of the impact. This change is partially reflected in the evolution of the strain energies associated with bending and membrane-stretching, whereby water-backing hinders membrane-stretching for small drop heights.

In the study of a fluid-structure interaction problem, the implementation of out-of-plane DIC with a top-view camera may help mitigate potential confounds associated with water splash, surface waves, air ventilation, and image blurring due to limited camera depth-of-field. Here, another possible experimental setup for the quantification of the plate deflection involves the use of a regular in-plane DIC, where a side-view camera could capture the in-plane displacement of a speckle pattern on the front side of the plate. However, images of the speckle pattern acquired by a side-view camera are likely subject to optical distortions caused by water splashes and surface waves, which could lead to a higher level of uncertainty in the deflection measurement.

We used PIV to measure the flow velocity associated with the impact, from which we reconstructed the pressure field by integrating Poisson's equation. In agreement with our expectations, we identify a high-velocity flow region below the plate, at the onset of the impact. Therein, we record large values of the pressure field, due to the sudden acceleration of the fluid. As time progresses and the plate attains larger deflection, the velocity decreases and the pressure values become smaller than the atmospheric pressure, due to the plate deceleration. Examining the hydrodynamic loading on the plate, we discover a rich temporal evolution, characterized by a pressure peak that travels back and forth along the span of the plate as it slowly diffused during the

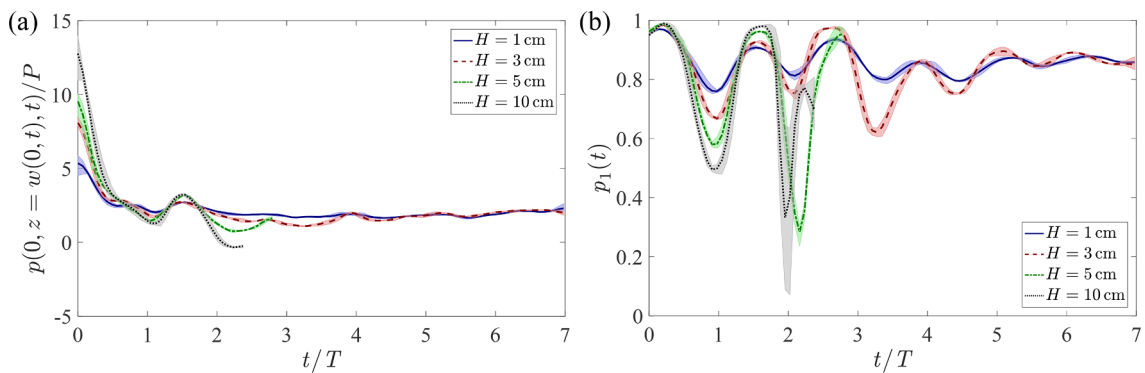


Fig. 15. (a) Hydrodynamic pressure at the mid-span of the plate for all drop heights. (b) Projection of the spatial distribution of the hydrodynamic pressure to the fundamental mode shape $m(x)$ as a function of time. The shaded areas are lower and upper bounds, based on three repetitions, and lines represent mean values.

impact. In contrast with the plate deflection, the modal contribution factor for the hydrodynamic loading oscillates throughout the impact, indicating the presence of multiple modes.

The proposed experimental approach provides for the first time the possibility to simultaneously study flow physics and structural response. A combined experimental scheme is critical to the study of fluid-structure interaction during water-backed impact, where understanding of the physics of the impact could be advanced through the precise quantification of the hydrodynamic loading and the concurrent plate deflection. This is in sharp contrast with the state-of-the-art, which exclusively relied on the use of sensors to obtain point-wise readings of contact forces and local strain. Although these measurements are helpful in the characterization of the material response of marine and aerospace panels [1,2], they do not allow for pinpointing the physical mechanisms underlying low-speed impact response of water-backed plates.

While a combined DIC/PIV approach may advance our understanding of unsteady fluid-structure interactions, the present work is not free of technical limitations. The reconstruction of mechanical deformation from out-of-plane DIC data is known to be challenging [33], leading to a relative error of up to 5% for static rigid body movement [33]. The impulsive nature of our experiments along with potential three-dimensional deformation would induce further uncertainty. We also acknowledge that the calibration of the reconstruction algorithm is only at the level of a pixel, which might be improved by using strain gages rather than image tracking in the calibration phase. Another drawback of our approach lies in the underestimation of the velocity gradient below the mid-span of the plate following the onset of the impact. Similar issues associated with PIV measurements have been reported in the literature for the study of water entry problems [29,39]. This issue can be possibly mitigated using PIV systems with higher camera acquisition frequency, as evidenced by a numerical assessment of the accuracy of PIV-based pressure reconstruction on a synthetic dataset of the impact of a rigid wedge on the water surface [46]. Therein, it was demonstrated that the peak hydrodynamic pressure on the wetted surface of the wedge could be underpredicted for low acquisition frequency, and the accuracy of pressure reconstruction could be significantly improved with increased acquisition frequency. Based on analysis presented in [46], it is tenable that increasing the acquisition frequency to several kHz would reduce the discrepancy between PIV and direct measurement within 10%.

Building upon the current experimental framework, we envision several lines of future inquiry to further improve our understanding of low speed impact of water-backed plates. First, the role of added mass of water could be better quantified by testing a range of impactor weights and plate geometries, toward shaping the interplay between the inertia of the water and the inertia associated with the impactor and the dry plate. Second, the proposed technique should be expanded to study low-speed impact at varying temperatures on composite materials to help the quantification of material damage in extreme environments. Finally, hypothesis-driven experiments should be conducted to validate existing mathematical model or inform the development of new theoretical models for low-speed impact of water-backed panels.

Data availability

The raw data required to reproduce these findings are available to download from <https://doi.org/10.17632/bvhgjy8y5z.1#file-1f2d80d1-cda3-40ae-8612-ed64b390887f>. The processed data required to reproduce these findings are available to download from <https://doi.org/10.17632/ksshkw2529.1#file-58c46983-d07b-43fb-ba6d-0be697b50f05>.

Declaration of Competing Interest

The authors declare no conflict of interest.

Acknowledgements

This work was supported by the Office of Naval Research through Grant No. N00014-18-1-2218 with Dr. Yapa D. S. Rajapakse as program manager. The authors thank Riccardo Consolo for his help with assembling the experimental setup.

References

- [1] Langella A, Lopresto V, Caprino G. Low temperature impact of composite hull wall with floating rigid body. In: 20th International Conference on Composite Materials (ICCM20); 2016.
- [2] Lopresto V, Langella A, Papa I. Dynamic load on composite laminates in the presence of water. *Polym Eng Sci* 2017;57(6):613–20. <https://doi.org/10.1002/pen.24563>.
- [3] Endo H, Yago K. Time history response of a large floating structure subjected to dynamic load. *J Soc Naval Arch Japan* 1999;1999(186):369–76. <https://doi.org/10.2534/jjasnaoe1968.1999.186.369>.
- [4] Kashiwagi M. Transient responses of a VLFS during landing and take-off of an airplane. *J Mar Sci Technol* 2004;9(1):14–23. <https://doi.org/10.1007/s00773-003-0168-0>.
- [5] Jin J, Xing J. Transient dynamic analysis of a floating beam-water interaction system excited by the impact of a landing beam. *J Sound Vib* 2007;303(1):371–90. <https://doi.org/10.1016/j.jsv.2007.01.026>.
- [6] Kwon Y, Owens A, Kwon A. Experimental study of impact on composite plates with fluid-structure interaction. *Int J Multiphys* 2016;4(3):259–71. <https://doi.org/10.1260/1750-9548.4.3.259>.
- [7] Kwon YW, Owens AC, Attaf B, editor. *Advances in Composite Materials*. IntechOpen; 2011. Ch. 15.
- [8] Kwon Y, Conner R. Low velocity impact on polymer composite plates in contact with water. *Int J Multiphys* 2012;6(3):179–97. <https://doi.org/10.1260/1750-9548.6.3.179>.
- [9] Kwon YW, Violette MA, McCrillis RD, Didoszak JM. Transient dynamic response and failure of sandwich composite structures under impact loading with fluid structure interaction. *Appl Compos Mater* 2012;19(6):921–40. <https://doi.org/10.1007/s10443-012-9249-8>.
- [10] South TJ, Kwon YW. Chapter 12 – low-speed impact on composite box containing water. In: Mouritz AP, Rajapakse YD, editors. *Explosion Blast Response of Composites*. Woodhead Publishing; 2017. p. 317–44. <https://doi.org/10.1016/B978-0-08-102092-0.00012-1>.
- [11] Reid S, Hendry S. Impact response of fluid-backed metal beams. *Comput Struct* 1985;20(1):321–38 Special Issue: Advances and Trends in Structures and Dynamics. doi:[https://doi.org/10.1016/0045-7949\(85\)90082-3](https://doi.org/10.1016/0045-7949(85)90082-3).
- [12] Owens A, Didoszak J, Kwon A, Kwon Y. Underwater impact of composite structures. In: ASME 2010 Pressure Vessels and Piping Division/K-PVP Conference, American Society of Mechanical Engineers; 2010. p. 231–240. <https://doi.org/10.1115/PVP2010-25065>.
- [13] Korobkin A. Unsteady hydroelasticity of floating plates. *J Fluids Struct* 2000;14(7):971–91. <https://doi.org/10.1006/jfls.2000.0304>.
- [14] Sturova IV. Unsteady behavior of an elastic beam floating on the surface of an infinitely deep fluid. *J Appl Mech Tech Phys* 2006;47(1):71–8. <https://doi.org/10.1007/s10808-006-0010-7>.
- [15] Shams A, Lopresto V, Porfiri M. Modeling fluid-structure interactions during impact loading of water-backed panels. *Compos Struct* 2017;171:576–90. <https://doi.org/10.1016/j.compstruct.2017.02.098>.
- [16] Abrate S. Impact on composite plates in contact with water. *Proc Eng* 2014;88:2–9 Part of Special Issue: International Symposium on Dynamic Response and Failure of Composite Materials, DRaF2014. doi:<https://doi.org/10.1016/j.proeng.2014.11.119>.
- [17] Abrate S. Impact on composite plates in contact with water. In: Lopresto V, Langella A, Abrate S, editors. *Dynamic Response and Failure of Composite Materials and Structures*. Woodhead Publishing; 2017. p. 183–216. <https://doi.org/10.1016/B978-0-08-100887-4.00006-8>.
- [18] LeBlanc J, Shukla A. Dynamic response and damage evolution in composite materials subjected to underwater explosive loading: an experimental and computational study. *Compos Struct* 2010;92(10):2421–30. <https://doi.org/10.1016/j.compstruct.2010.02.017>.
- [19] Ren L, Ma H, Shen Z, Wang Y. Blast response of water-backed metallic sandwich panels subject to underwater explosion – experimental and numerical investigations. *Compos Struct* 2019;209:79–92. <https://doi.org/10.1016/j.compstruct.2018.10.082>.
- [20] Chu TC, Ranson WF, Sutton MA. Applications of digital-image-correlation techniques to experimental mechanics. *Exp Mech* 1985;25(3):232–44. <https://doi.org/10.1007/BF02325092>.
- [21] Pan B, Qian K, Xie H, Asundi A. Two-dimensional digital image correlation for in-plane displacement and strain measurement: a review. *Meas Sci Technol* 2009;20(6):062001. <https://doi.org/10.1088/0957-0233/20/6/062001>.
- [22] Arora H, Hooper PA, Dear JP. Dynamic response of full-scale sandwich composite structures subject to air-blast loading. *Compos Part A: Appl Sci Manuf* 2011;42(11):1651–62. <https://doi.org/10.1016/j.compositesa.2011.07.018>.
- [23] Gardner N, Wang E, Shukla A. Performance of functionally graded sandwich composite beams under shock wave loading. *Compos Struct* 2012;94(5):1755–70. <https://doi.org/10.1016/j.compstruct.2011.12.006>.

- [24] Namala KK, Mahajan P, Bhatnagar N. Digital image correlation of low-velocity impact on a glass/epoxy composite. *Int J Comput Methods Eng Sci Mech* 2014;15(3):203–17. <https://doi.org/10.1080/15502287.2014.882441>.
- [25] Flores M, Mollenhauer D, Runatunga V, Beberniss T, Rapking D, Pankow M. High-speed 3D digital image correlation of low-velocity impacts on composite plates. *Compos Part B: Eng* 2017;131:153–64. <https://doi.org/10.1016/j.compositesb.2017.07.078>.
- [26] Gauch E, LeBlanc J, Shukla A. Near field underwater explosion response of polyurea coated composite cylinders. *Compos Struct* 2018;202:836–52. <https://doi.org/10.1016/j.compstruct.2018.04.048>.
- [27] Pickering CJD, Halliwell NA. Laser speckle photography and particle image velocimetry: photographic film noise. *Appl Opt* 1984;23(17):2961–9. <https://doi.org/10.1364/AO.23.002961>.
- [28] Raffel M, Willert CE, Wereley S, Kompenhans J. *Particle image velocimetry: a practical guide*. 2nd ed. Springer; 2007.
- [29] Porfiri M, Shams A. Pressure reconstruction during water impact through particle image velocimetry: methodology overview and applications to lightweight structures. In: Lopresto V, Langella A, Abrate S, editors. *Dynamic response and failure of composite materials and structures*. Woodhead Publishing; 2017. p. 395–416. doi:<https://doi.org/10.1016/B978-0-08-100887-4.00013-5>.
- [30] van Oudheusden BW. PIV-based pressure measurement. *Meas Sci Technol* 2013;24(3):032001<https://doi.org/10.1088/0957-0233/24/3/032001>.
- [31] Pan Z, Whitehead J, Thomson S, Truscott T. Error propagation dynamics of PIV-based pressure field calculations: how well does the pressure Poisson solver perform inherently? *Meas Sci Technol* 2016;27(8):084012<https://doi.org/10.1088/0957-0233/27/8/084012>.
- [32] Zhang P, Peterson SD, Porfiri M. Combined particle image velocimetry/digital image correlation for load estimation. *Exp Thermal Fluid Sci* 2019;100:207–21. <https://doi.org/10.1016/j.expthermflusci.2018.09.011>.
- [33] Quan C, Tay CJ, Sun W, He X. Determination of three-dimensional displacement using two-dimensional digital image correlation. *Appl Opt* 2008;47(4):583–93. <https://doi.org/10.1364/AO.47.000583>.
- [34] Réthoré J, Morestin F, Lafarge L, Valverde P. 3D displacement measurements using a single camera. *Opt Lasers Eng* 2014;57:20–7. <https://doi.org/10.1016/j.optlaseng.2014.01.009>.
- [35] Palchesko RN, Zhang L, Sun Y, Feinberg AW. Development of polydimethylsiloxane substrates with tunable elastic modulus to study cell mechanobiology in muscle and nerve. *PLoS ONE* 2012;7(12):1–13. <https://doi.org/10.1371/journal.pone.0051499>.
- [36] Hocheng H, Chen C-M, Chou Y-C, Lin C-H. Study of novel electrical routing and integrated packaging on bio-compatible flexible substrates. *Microsyst Technol* 2009;16(3):423. <https://doi.org/10.1007/s00542-009-0930-2>.
- [37] Johnston ID, McCluskey DK, Tan CKL, Tracey MC. Mechanical characterization of bulk Sylgard 184 for microfluidics and microengineering. *J Micromech Microeng* 2014;24(3):035017<https://doi.org/10.1088/0960-1317/24/3/035017>.
- [38] Wang Z, Volinsky AA, Gallant ND. Crosslinking effect on polydimethylsiloxane elastic modulus measured by custom-built compression instrument. *J Appl Polym Sci* 2014;131(22). <https://doi.org/10.1002/app.41050>.
- [39] Russo S, Jalalisendi M, Falcucci G, Porfiri M. Experimental characterization of oblique and asymmetric water entry. *Exp Thermal Fluid Sci* 2018;92:141–61. <https://doi.org/10.1016/j.expthermflusci.2017.10.028>.
- [40] Blaber J, Adair B, Antoniou A. Ncorr: open-source 2D digital image correlation Matlab software. *Exp Mech* 2015;55(6):1105–22. <https://doi.org/10.1007/s11340-015-0009-1>.
- [41] Thielicke W, Stamhuis E, user-friendly PIVlab-towards. affordable and accurate digital particle image velocimetry in MATLAB. *J Open Res Software* 2014;2(1). <https://doi.org/10.5334/jors.bl>.
- [42] Caprino G, Lopresto V, Scarponi C, Briotti G. Influence of material thickness on the response of carbon-fabric/epoxy panels to low velocity impact. *Compos Sci Technol* 1999;59(15):2279–86. [https://doi.org/10.1016/S0266-3538\(99\)00079-2](https://doi.org/10.1016/S0266-3538(99)00079-2).
- [43] Lopresto V, Melito V, Leone C, Caprino G. Effect of stitches on the impact behaviour of graphite/epoxy composites. *Compos Sci Technol* 2006;66(2):206–14. <https://doi.org/10.1016/j.compscitech.2005.04.029>.
- [44] Shams A, Lopresto V, Porfiri M. Impact loading on marine panels: modeling the effect of water backing. *Proc Eng* 2016;167:18–22 Part of Special Issue: International Symposium on Dynamic Response and Failure of Composite materials, DRaF2016. doi:<https://doi.org/10.1016/j.proeng.2016.11.664>.
- [45] Mansfield EH. Chapter VIII – approximate methods in large-deflexion analysis. In: Mansfield EH, editor. *The Bending and Stretching of Plates*, vol. 6 of International Series of Monographs on Aeronautics and Astronautics: Solid and Structural Mechanics, Pergamon; 1964, p. 114–127.<https://doi.org/10.1016/B978-1-4831-9763-0.50014-8>.
- [46] Facci AL, Panciroli R, Ubertini S, Porfiri M. Assessment of PIV-based analysis of water entry problems through synthetic numerical datasets. *J Fluids Struct* 2015;55:484–500. <https://doi.org/10.1016/j.jfluidstructs.2015.03.018>.